WILEY | Hindawi

Research Article

Frequency Regulation of Nonlinear Power Systems using Neural Network Observer-Based Optimized Resilient Controller

Vivek Patel [ID]**, Dipayan Guha** [ID]**, and Shubhi Purwar** [ID]

Electrical Engineering Department, Motilal Nehru National Institute of Technology Allahabad, Prayagraj, India

Correspondence should be addressed to Dipayan Guha; dipayan@mnnit.ac.in

This study introduces a resilient frequency controller for nonlinear interconnected power systems to counteract endogenous/exogenous system disturbances. A neural network-based observer (NNO) is intended to estimate lumped system disturbances, such as unmodelled dynamics and unknown disturbances. The estimated NNO's output is incorporated with a second-order sliding mode controller (SOSMC) to minimize chattering in the control effort and improve the nominal performance of the undertaken plant. The design parameters of SOSMC have been optimally identified by applying Harris hawk optimization (HHO), exercising integral error-based objective function. HHO has demonstrated superior tuning capabilities than other well-known optimization methodologies in terms of convergence rate and transient measurements of system outputs. The asymptotic convergence of estimated error and overall stability of the system has been established employing the Lyapunov argument. System outputs are compared with the results reported in the literature to validate the efficacy of the proposed resilient frequency controller. Presented results showcase the mastery of the applied NNO-based SOSMC over its counterparts in weaker chattering, fast disturbance rejection, and a high degree of robustness against endogenous/exogenous disturbances.

1. Introduction

Due to the continuum shrinking of conventional fossil fuel resources, escalating fuel prices, geographical constraints, global warming, and increasing load demand, low-inertia inverter-based renewable energy resources (RERs) that are integrated into the existing power grid have been progressively increased. Among the RERs, wind power generator (WPG) is widely utilized due to their high energy conversion efficiency and relatively cheaper than photovoltaic system [1]. In the future, wind energy is predicted to meet a large portion of global energy needs. Several huge offshore wind farms have already been built and are connected to the electrical grid. Wind energy farms are predicted to produce 40% of all energy in the United States by 2030.

Grid frequency stability and power system operation grow increasingly difficult as large-scale wind farms are developed. The frequency stability in the region is impacted by the randomness and nondispatchable characteristics of wind power [2]. WPGs contribute little or nothing to frequency stability. Due to the use of power electronic converters, modern wind farms are mostly isolated from grid frequency and do not contribute to power system inertia. Only synchronously connected rotating generators and motors give apparent inertia and help to maintain frequency stability. Hence, large penetration of variable renewable energy reduces the power system's apparent inertia, which can cause undesired frequency variation, voltage instability, low-grade power quality, and reliability obstruction. Moreover, unpredictable load variations may cause the frequency to droop from its theoretical value (50 Hz/60 Hz). Excessive frequency droop may cause instability/blackout of the entire system. To preserve frequency stability under extensive penetration of WPGs, the design and realization of resilient frequency controllers are in high demand [2, 3].

1.1. Litrature Survey. To alleviate frequency oscillations caused by sudden load variations and/or RERs transient, various control methodologies have been reported in the

state of the art, including metaheuristic-based classical controllers [4–6], robust controllers [7], fractional-order aided controllers [8–10], intelligent controllers [11, 12], and so on. According to a study of the existing literature, the performance of conventional controllers in frequency regulation of power systems with/without RERs incorporated has been widely used [2, 3]. An output feedback-based optimal control for in frequency regulation of reduced power systems model has been discussed in reference [13]. In the above-cited works, traditional controllers considerably improve system dynamics. However, its performance deteriorates with parametric uncertainty, unmodelled dynamics, and unknown/uncertain external perturbations. Fuzzy-aided controllers may overcome the above-said limitations and increases stability degree. However, the design of a fuzzy-aided controller requires high training data set, a suitable selection of input control parameters (e.g., membership function and scaling factors), and is computationally intensive [6].

Robust control algorithms are necessary to achieve good dynamic performance throughout various operating conditions and severe loading fluctuation. The sliding mode controller (SMC) has appeared as one of the most powerful robust controllers for uncertain nonlinear interconnected power systems (NIPSs) due to its inherent robust operation against structured vulnerabilities and considerable improvement in the system dynamics [14, 15]. In frequency regulation of power systems with or without RPRs, the SMC has received much attention. In references [16–18], SMC's ability to provide quick frequency response was highlighted, leaving high-frequency oscillation (chattering) in controller's output. In reference [19], nonlinear SMLFC for power systems is presented. A disturbance-observer based SMLFC is discussed in references [20, 21]. Considering the above-said troubled situation, the SMC's performance has been improved by integrating linear/nonlinear disturbance observers [21, 22]. Sliding mode observer-based SMLFC has been presented in reference [23].

According to the above study, a frequency controller is developed for a rationalised power system that includes or excludes renewable energy inputs. After that, the performance of the controller is examined, considering system's nonlinearities (governor dead band (GDB) and generation rate constraints (GRC)) as well as parametric uncertainties. The research mentioned above did not consider the system's nonlinearities and uncertainties while building the system model. Chattering is generally acknowledged to be a major impediment to the traditional SMC. A literature assessment also reveals that a trade-off between chattering and robustness is required to increase SMC's performance [24, 25].

Disturbance compensation was used by power system researchers to reduce the impact of system's nonlinearities and uncertainties. Thus, the planning a state and disturbance estimator with an effective approximation is a fundamental for achieving a superior control structure. The neural network is the most used estimation technique of the system uncertainties/dynamics, despite its excellent approximation analysis and adaptive learning capabilities. In reference [26], the performance of the neural network-aided integral SMC

(NN-ISMC) was examined, and it was found to be more effective than conventional SMC in improving chattering tasks [25, 26]. In reference [27], NN-based nonlinear SMC has been applied for frequency regulation of a power system. NN was used to estimate unmatched plant uncertainties. In reference [28], NN-based fractional-order ISMC is described. However, the drawback of this literature was the controller parameter was taken by trial-error method, and the chattering was not eliminated in controller output. A resilient frequency controller has been attempted to counterbalance power-frequency oscillations of the studied power system, taking into account the benefits of neural networks and second-order sliding mode controllers (SOSMCs).

1.2. Motivations. Given the preceding discussion, the following attributes encourage the examination of the present work:

(i) To deliver a stable and consistent electrical power to end-users, the analysis of a realistic (including parametric uncertainty and nonlinearities) nonlinear interconnected power systems (NIPSs) with renewable energy resources integrated may be carried out.

(ii) Estimation of plant uncertainty is needed for enriching the controller performance.

(iii) The traditional SMC suffers from a chattering problem. Therefore, implementing a resilient frequency controller for stable power systems operation with the minimum chattering is imperative.

However, to tackle the frequency regulation problem, a neural network observer (NNO) and second-order SMC (SOSMC) are fused due to their accuracy and extensive application. The NNO is best suited to predict system variables reliably, even in any power system vulnerability. The NNO may also get approximate realizations of plant dynamics in frequency regulation support based on its input-output history when subjected to uncertain nature constrained renewable power integration. In SOSMC, a control input's derivative is used to perform a second-order derivative of the sliding variable. The control input's derivative is discontinuous. However, the control input's integration is continuous, making the control input less chattering. As a result, wear and tear issues in the governor valve actuator in the steam turbine servo system are reduced.

1.3. Contributions. As a result of the abovementioned aspects, the significant contributions in this study are listed below.

(i) Design and access the SOSMC's frequency control performance in a nonlinear interconnected power system (NIPS).

(ii) The SOSMC's impacts are evaluated using a power system model that includes both thermal and wind power plants.

(iii) The impact of power system's nonlinearities such as GDB and GRC on controller performance has been examined.

(iv) NNO is designed and used to estimate system states and lumped unknown/uncertain plant mismatches, and an improved control law/effort is generated based on this estimation.

(v) Harris hawk optimization (HHO) is applied to tune the parameter of SOSMC and compared with salp swarm algorithm (SSA), particle swarm optimization (PSO), deferential evaluation (DE), and crow search algorithm (CSA). The tuning competence of HHO algorithm has been measured in terms of convergence rate with PSO, DE, CSA, and SSA under identical simulation environment.

(vi) A comparison analysis was conducted to verify the superiority of the applied optimized SOSMC over the NN-ISMC [26] in terms of system performance, chattering, and robustness against system mismatches.

1.4. Organization of the Study. The rest of the study is laid out as follows. Section 2 presents the modelling of the analysed NIPS with a wind power system. Section 3 discusses the implementation and analysis of NNO-based SOSMC. Section 4 contains the simulation outputs and a comparison discussion. The conclusion of the current work is described in Section 5.

2. System Modeling

To quantify the mastery of the proposed NNO-SOSMC, a thermal power plant having wind power plant integrated has been undertaken to perform the present investigation. Figure 1 depicts the linearized model of the studied test system. To carry out the investigation on the realistic domain, detailed mathematical models of WTG, including wind aerodynamics, coupling shaft, and generator, have been derived and considered for the assessment of the proposed controllers' performance. The GRC and GDB as physical constraints are involved in the model to assess the proposed controller's efficacy in coping with physical constraints. The dynamical model of the studied system is represented by the following differential equations:

$$
\left.
\begin{aligned}
\Delta \dot{f}_i\,(t) &= -\frac{1}{T_{pi}}\Delta f_i(t) + \frac{K_{pi}}{T_{pi}}\Delta P_{gi}(t) - \frac{K_{pi}}{T_{pi}}\Delta P_{ij}(t) - \frac{K_{pi}}{T_{pi}}\Delta P_{di}(t) \\[2mm]
\Delta \dot{p}_{ti}\,(t) &= \left\{-\Delta P_{ti}(t) + \Delta X_{gi}(t)\right\}\frac{1}{T_{ti}} + \frac{n_2}{T_{gi}}\left\{-\frac{\Delta f_i(t)}{R} - \Delta E_i(t) + u(t)\right\}\frac{1}{T_{ti}} \\[2mm]
\Delta \dot{X}_{gi}\,(t) &= -\frac{1}{T_{gi}}\Delta X_{gi}(t) + \frac{1}{T_{gi}}\left\{n_1 - \frac{n_2}{T_{gi}}\right\}\left\{-\frac{\Delta f_i(t)}{R_i} - \Delta E_i(t) + u(t)\right\} \\[2mm]
\Delta \dot{E}_i\,(t) &= K_{ei}B_i\Delta f_i(t) + K_{ei}\Delta P_{tie_{ij}}(t) \\[2mm]
\Delta \dot{P}_{tie_{ij}}\,(t) &= 2\pi T_{i,j}\left(\Delta f_i(t) - \Delta f_j(t)\right) \\[2mm]
&\text{where } i, j = 1, 2, \quad i \neq j
\end{aligned}
\right\}.
\tag{1}
$$

where Δf_i, ΔP_{ti}, $\Delta P_{tie_{ij}}$, ΔX_{gi}, and ΔE_i are the changes in area frequency, nonreheat turbine output, tie-line interchange power, governor valve position, and integral control effort, respectively; $\Delta P_{di}(t)$ and P_w are the deviation in the load demand and uncertain output power of WTG, respectively; T_{gi}, T_{pi}, and T_{ti} are the time constants of speed governor, power system, and turbine, respectively; T_{12} is the time constant of tie-line. Table 1 provides the nominal values of the thermal power system.

2.1. Wind Turbine Generator (WTG) Model. A variable speed WTG system model, as presented in Figure 1, is obtained to quantify the performance of proposed NNO-SOSMC
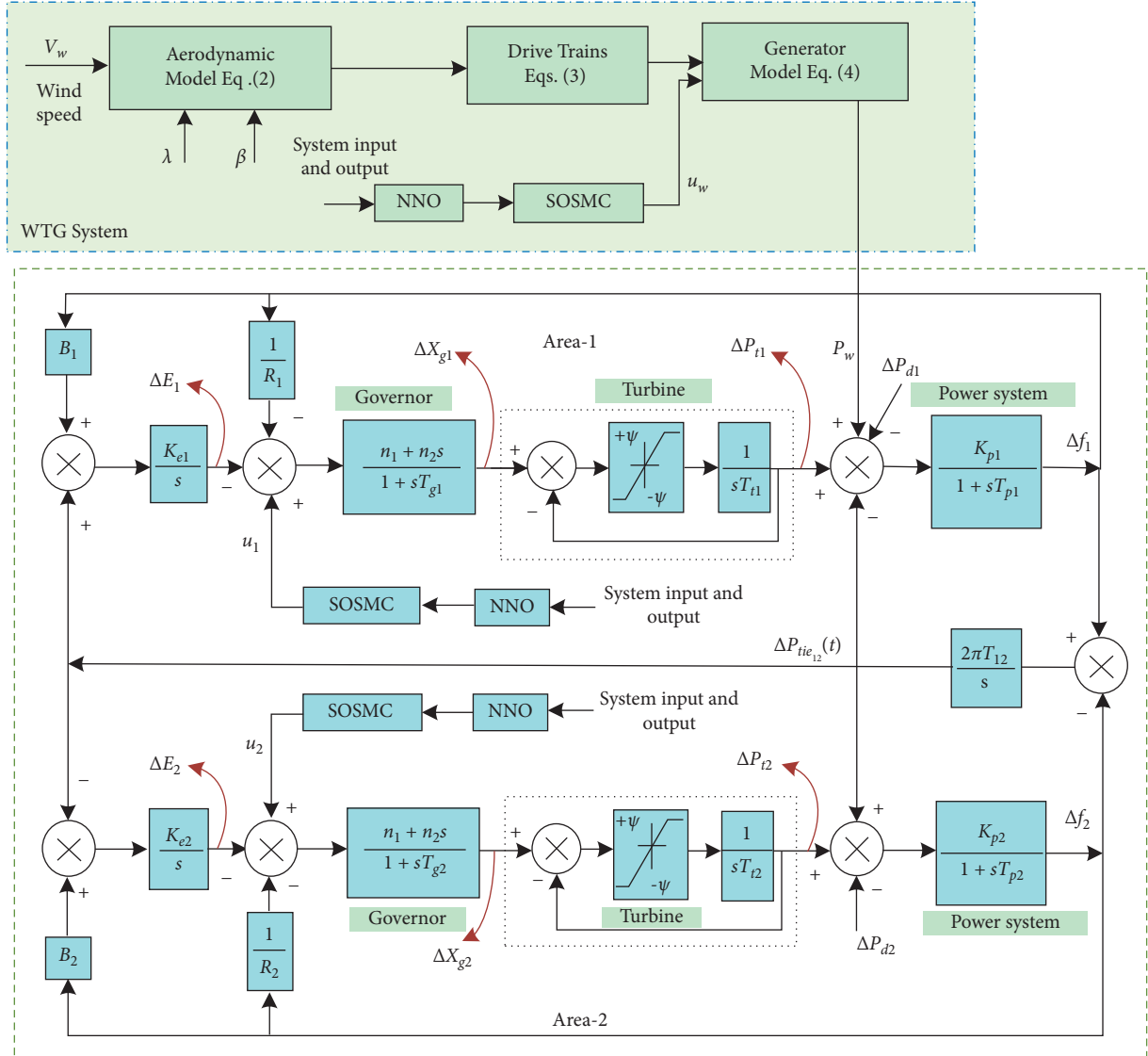
FIGURE 1: Two-area nonlinear interconnected power system (test system 1).

against the uncertain/unknown wind power output. The mechanical power output of wind aerodynamic is given by the following equation:

$$P_m = \frac{1}{2}\rho A_b V_w^3 C_P(\lambda, \beta)$$

$$\text{where,} \begin{cases} C_P = c_1\left(\frac{c_2}{\lambda_k} - c_3\beta - c_4\right)\exp\left(\frac{-c_5}{\lambda_k}\right) + c_6\lambda \\[3mm] \frac{1}{\lambda_k} = \frac{1}{\lambda + 0.08\beta} - \frac{0.03}{\beta^3 + 1} \end{cases}, \quad (2)$$

where ρ is the air density (kg/m^3), V_w is the incoming wind speed (m/s^2), A_b is the WT blade swept area (m^2), and C_p is the power coefficient [19, 25].

The model of coupling shaft is given by the following equations:

$$\begin{aligned} \dot{\omega}_t(t) &= \left(-\frac{B_t + B_{sh}}{I_t}\right)\omega_t(t) + \left(\frac{B_{sh}}{I_t}\right)\omega_g(t) - \frac{\delta_{tg}(t)}{I_t} + \left(\frac{1}{I_t}\right)T_r, \\[2mm] \dot{\omega}_g(t) &= \left(\frac{B_{sh}}{2I_g}\right)\omega_t(t) - \left(\frac{B_g + B_{sh}}{I_g}\right)\omega_g(t) + \frac{\delta_{tg}(t)}{N_g I_g} - \left(\frac{1}{I_g}\right)T_g(t) \\[2mm] \dot{\delta}_{tg}(t) &= K_{sh}\left(\omega_t(t) - \frac{\omega_g(t)}{N_g}\right), \end{aligned} \Bigg\}, \quad (3)$$

where T_g and T_r are the torque on generator and rotor side, respectively; I_g and I_t are the inertia of generator and rotor side, respectively; B_g and B_t are the rotor damping coefficients of generator, and turbine, respectively; B_{sh} and K_{sh} are the damping and spring constant of the shaft, respectively; N_g is the gear-train ratio; ω_g and ω_t are the generator speed and rotor speed, respectively; δ_{tg} is the shaft stiffness of the two-mass model. An asynchronous generator has been

TABLE 1: Thermal power system parameters.

K_{p1}, K_{p2}	120	T_{t1}, T_{t2}	0.3	B_1, B_2	0.425	K_{i1}, K_{i2}	1.2	n_1	0.8
T_{p1}, T_{p2}	20	T_{g1}, T_{g2}	0.08	T_{12}	0.05	R_1, R_2	2.4	n_2	$-(0.2/\pi)$

described by a first-order differential equation, as given in equation (4). The generator power $P_w = T_g \times \omega_g$ is deliberated as a net WTG's power output [20, 28].

$$\dot{T}_g = -\frac{1}{\tau_g}T_g + \frac{u_w}{\tau_g}, \tag{4}$$

where τ_g is the generator's time constant.

The state-space model of the investigated power system, including dynamic variation in system parameter, is obtained as in the following equation:

$$\dot{x}(t) = A_1 x(t) + B_1 u(t) + B_{d1}\Delta P(t), \tag{5}$$

where $\begin{cases} A_1 = (A + \Delta A), B_1 = (B + \Delta B), B_{d_1} = (B_d + \Delta B_d) \\ x(t) = \end{cases}$

$[\Delta f_1 \quad \Delta P_{t1}\Delta G_{g1}\Delta E_1\Delta f_2\Delta P_{t2}\Delta G_{g2}\Delta E_2\Delta P_{tie12} \quad \Delta\omega_t\Delta\omega_r\Delta\delta_{tr}$

$\Delta T_r]^T \in \mathbb{R}^{13\times 1} u(t) = [u_1 \quad u_2 \quad u_w] \in \mathbb{R}^{3\times 1}\Delta P(t) =$

$[\Delta P_{d1} \quad \Delta P_{d2} \quad P_w \quad T_g]^T \in \mathbb{R}^{4\times 1}$, $x(t)$ is the system states, $u(t)$ is the states, and $\Delta P(t)$ is the disturbance input of the system. Including the parameter uncertainties, equation (5) can be written as follows:

$$\left.\begin{aligned} \dot{x}(t) &= (A + \Delta A)x(t) + (B + \Delta B)u(t) + (B_d + \Delta B_d)\Delta P(t) \\ \dot{x}(t) &= Ax(t) + Bu(t) + B_d\Delta P(t) + \Delta Ax(t) + \Delta Bu(t) + \Delta B_d\Delta P(t) \end{aligned}\right\}, \tag{6}$$

where $A \in \mathbb{R}^{13\times 13}$ is the system matrix, $B \in \mathbb{R}^{13\times 13}$ is the input matrix, $B_d \in \mathbb{R}^{13\times 4}$ is the disturbance matrix, computed at nominal value, and $\Delta Ax(t)$, $\Delta Bu(t)$, and $\Delta B_d\Delta P(t)$ show the parametric uncertainties.

GRC bounds the maximum generated power. The steam turbine's output with GRC can be described [25] as follows:

$$\Delta P_{ti}\begin{cases} -\dfrac{1}{T_{ti}}\displaystyle\int \psi dt & \alpha(t) <-\psi, \\[2ex] \dfrac{1}{T_{ti}}\displaystyle\int \alpha(t)dt & |\alpha(t)| \le -\psi, \\[2ex] \dfrac{1}{T_{ti}}\displaystyle\int \psi dt & \alpha(t) > \psi. \end{cases} \tag{7}$$

Therefore, $\alpha(t) = [\Delta G_{gi}(t) - \Delta P_{ti}(t)]$ and $\psi > 0$. Considering GRC, equation (6) is modified as follows:

$$\begin{aligned} \dot{x}(t) = Ax(t) &+ Bu(t) + B_d\Delta P(t) + \Delta Ax(t) \\ &+ \Delta Bu(t) + \Delta B_d\Delta P(t)\varphi(t). \end{aligned} \tag{8}$$

where $\varphi(t)$ in equation (8) denotes the impact of GRC. Therefore, the state-space model of the studied power system is described as follows:

$$\left.\begin{aligned} \dot{x}(t) &= Ax(t) + Bu(t) + d(t) \\ \text{where } d(t) &= \Delta Ax(t) + \Delta Bu(t) + \Delta B_d\Delta P(t) + \phi(t) + B_d\Delta P(t) \end{aligned}\right\}, \tag{9}$$

where $d(t)$ symbolizes the lumped unknown plant uncertainties and nonlinearities, and A, B, and H matrices are the matrices computed for test system 1 described in Appendix. The proposed control technique for the system (equation (9)) is presented in the next section.

3. Control Strategy

A neural network-based observer (NNO) is developed in this section to effectively estimate limped plant uncertainty [29–32]; later, the estimated output is incorporated with second-order SMC for increasing speed of response and minimizing chattering. The design of the proposed method is not distinctive and can be realized on four-area power system. The schematic diagram of proposed control structure is shown in Figure 2.

3.1. Neural Network Observer. The Chebyshev neural network is a useful tool for estimating vulnerabilities with a basic topological structure that fills the gap between system stability and the uncertain boundary value. The following recursive formula can be used to define Chebyshev polynomials equation (10) [29, 30].

$$\begin{aligned} P_{j+1} &= 2xP_j(x) - P_{j-1}(x), \\ P_0(x) &= 1, \end{aligned} \tag{10}$$

where $P_j(x)$ is the Chebyshev polynomial and j is the polynomial order.

The structure of neural network (NN) is revealed in Figure 3. The output of NN is described in the following equation:

$$\bar{d}(x) = w^T\phi(x,u) + \varepsilon(x), \tag{11}$$

where $\varepsilon(x)$ is the reconstruction error and $\|\varepsilon(x)\| \le \varepsilon_1$ is bounded. w is the ideal weight of NN.

The NN observer (NNO) for the system (equation (9)) is defined as follows:

$$\left.\begin{aligned} \dot{\hat{x}}(t) &= A\hat{x}(t) + Bu(t) + \hat{d}(t) + L(y(t) - \hat{y}(t)) \\ \hat{y}(t) &= C\hat{x}(t) \end{aligned}\right\}. \tag{12}$$

where $\hat{x}$ is the estimated state variable and $\hat{y}$ is the estimated output. The observer gain $L \in \mathbb{R}^{n\times m}$ is chosen such that the matrix $(A - LC)$ is a Hurwitz matrix [28]. Therefore, matrix (A, C) should be observable.
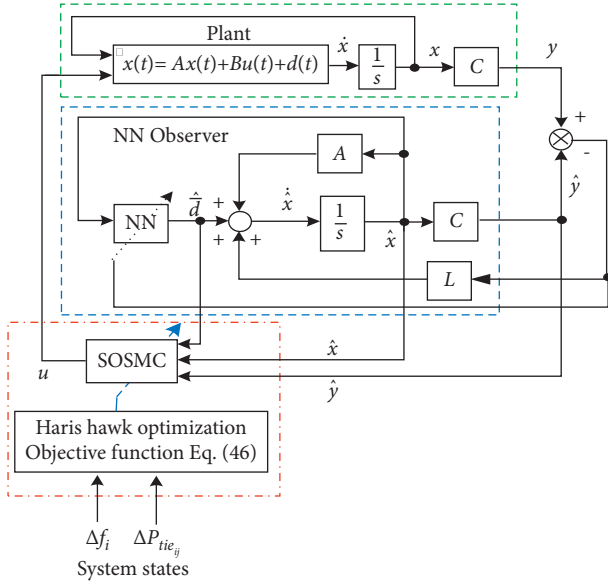
FIGURE 2: Schematic diagram of neural network observer with a controller.
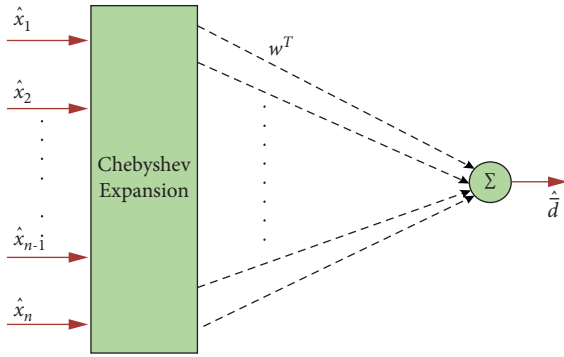

FIGURE 3: Structure of NN.

Assumption 1. The ideal weight $\|w\|_F \leq w_m$, where $\|\cdot\|_F$ represents the Frobenius norm.

The NN estimate of $\overline{d}(x)$ is described by using the following equation:

$$\widehat{\overline{d}}(x) = \widehat{w}^T \phi(x, t), \tag{13}$$

where $\widehat{w}$ is the estimated weight w, $\phi(x) = [1 P_j(x_1) \ldots P_j(x_{13})]^T$, and $j = 2$.

The NNO error dynamics is represented by the following equation:

$$e(t) = x(t) - \widehat{x}(t). \tag{14}$$

Using equations (9) and (12), the error dynamics of NNO is represented as follows:

$$\dot{e}(t) = (A - LC)e(t) + w^T(\phi(x, u) - \phi(\widehat{x}, u)) + \varepsilon(x) + \widetilde{w}^T \phi(\widehat{x}, u), \tag{15}$$

where $\widetilde{w} = w - \widehat{w}$, and $A_L = A - LC$, and the tuning law of weight $\widehat{w}$ is given in equation (31).

3.2. Design of Second-Order Sliding Mode Controller (SOSMC).

Sliding mode control (SMC) is identified as an effective, robust control technique due to its (i) fast dynamic response and (ii) insensitivity to variations in plant parameters and external disturbance. SOSMC is developed in this section to reduce chattering at the SMC output while maintaining the system's robustness. The main inadequacy of SMC is the chattering, which may cause damage to the final control element and makes the system more vulnerable to instability. Hence, it is required to quickly reduce/eliminate the chattering at the controller output effectively. Using a SOSMC can help reduce chattering and increase the overall robustness of a closed-loop control system. SOSMC design comprises two basic steps, similar to traditional SMC design: choosing a sliding surface and developing an effective control law. SOSMC has been designed based on the assumptions listed below [20, 27].

Assumption 2. The pair (A, B) is fully state controllable.

Assumption 3. $\|\dot{d}(t)\| \leq \overline{d}, \overline{d}(>0)$, where $\|\cdot\|$ indicates the standard vector norm, $d(t)$ is continuously differentiable function and bounded; that is, $\overline{d}$ is unknown but bounded positive constant.

Let the first-order sliding surface be

$$\sigma(t) = \alpha_1 \widehat{x}(t) - \int_0^t (\alpha_1 A - \alpha_1 B \alpha_2) \widehat{x}(\tau) d\tau, \tag{16}$$

where α_1 and α_2 are the controller design parameters with appropriate dimension, the matrix α_2 is to be selected to make sure the eigenvalues of $\text{Re}(A - B\alpha_2) < 0$, and $|\alpha_1 B| \neq 0$.

The prime objective of the SOSMC is to act on second-order derivative of the sliding surface $\sigma(t)$ rather than the first derivative as in standard-sliding mode, also retaining the advantage of the SMC, and SOSMC also has the advantage of eliminating the chattering effect [24]. The basic equality condition to design SOSMC is $\sigma(t) = \dot{\sigma}(t) = 0$.

To design the SOSMC, the first and second-order time derivatives of sliding surface (equation (16)) are obtained, as in equations (17) and (18), respectively:

$$\dot{\sigma}(t) = \alpha_1 \dot{\widehat{x}}(t) - (\alpha_1 A - \alpha_1 B \alpha_2) \widehat{x}(t) = 0. \tag{17}$$

$$\ddot{\sigma}(t) = \alpha_1 \ddot{\widehat{x}}(t) - (\alpha_1 A - \alpha_1 B \alpha_2) \dot{\widehat{x}}(t) = 0. \tag{18}$$

For designing SOSMC, the sliding function is chosen as shown in the following equation:

$$\sigma_n(t) = \dot{\sigma}(t) + \Upsilon \sigma(t), \quad [\Upsilon > 0], \tag{19}$$

where $\sigma_n(t)$ is the second-order sliding surface. Differentiating equation (19) yields

$$\dot{\sigma}_n(t) = \ddot{\sigma}(t) + \Upsilon \dot{\sigma}(t). \tag{20}$$

Substituting equations (17) and (19) into equation (20) gives

$$\left. \begin{array}{l} \dot{\sigma}_n\,(t) = \alpha_1 \ddot{\hat{x}}\,(t) - (\alpha_1 A - \alpha_1 B\alpha_2)\dot{\hat{x}}\,(t) + \Upsilon\left\{\alpha_1 \dot{\hat{x}}\,(t) - (\alpha_1 A - \alpha_1 B\alpha_2)\hat{x}(t)\right\} \\ \text{or } \dot{\sigma}_n\,(t) = \alpha_1\left\{A\dot{\hat{x}}\,(t) + B\dot{u}\,(t) + \dot{d}\,(t)\right\} - (\alpha_1 A - \alpha_1 B\alpha_2)\dot{\hat{x}}\,(t) + \Upsilon\dot{\sigma}(t) \end{array} \right\}. \tag{21}$$

The equality hitting condition $(\sigma_n(t)\dot{\sigma}_n(t) < 0)$ is assumed for designing the controller [20]:

$$\dot{\sigma}_n(t) = -\gamma_1 \sigma_n(t) - \gamma_2 \mathrm{sgn}\left(\sigma_n(t)\right). \tag{22}$$

From equations (21) and (22), we get

$$\dot{u}(t) = -\alpha_2 \dot{x}(t) - (\alpha_1 B)^{-1}\left[\|\alpha_1\|\overline{d}(t) + \Upsilon\dot{\sigma}(t) + \gamma_1 \sigma_n(t) + \gamma_2 \mathrm{sgn}\{\sigma_n(t)\}\right]. \tag{23}$$

It is impractical to know the exact boundary value $\overline{d}(t)$ of the lumped plant uncertainty. The controller is designed under the assumption that the uncertainties are unknown boundary. To refine the control effort, NNO is applied to estimate the upper bound of uncertain/unknown lumped plant uncertainty $\overline{d}(t)$.

Equation (23) is modified by using the Chebyshev-based NNO approximation:

$$\left. \begin{array}{l} \dot{u}(t) = -\alpha_2 \dot{x}(t) - (\alpha_1 B)^{-1}\left[\|\alpha_1\|\hat{\overline{d}}(t) + \Upsilon\dot{\sigma}(t) + \gamma_1 \sigma_n(t) + \gamma_2 \mathrm{sgn}\{\sigma_n(t)\}\right] \\ u(t) = \int_0^t \left[-\alpha_2 \dot{x}(t) - (\alpha_1 B)^{-1}\left(\|\alpha_1\|\hat{\overline{d}}(t) + \Upsilon\dot{\sigma}(t) + \gamma_1 \sigma_n(t) + \gamma_2 \mathrm{sgn}\left(\sigma_n(t)\right)\right)\right]d\tau \end{array} \right\}. \tag{24}$$

Equation (24) represents the control law of the proposed SOSMC integrated with NNO (NNO-SOSMC). The controller parameter is optimized by Harris hawk algorithm, which is given in Section 4. The stability analysis of the proposed controller is given in the next subsection.

3.3. Stability Analysis

Assumption 4. $|(w^T\phi(x) - \overline{d})| \leq \xi$, ξ is a positive constant.

Theorem 1. *Take Assumption 1–3 into account. Considering the system (equation (9)), sliding surface (equation (19)), and control law equation (24), if the system is stable, then weight update law for NN has the following form:*

$$\dot{\hat{w}} = \mathrm{T}\|k_1\|\phi\sigma_n^T - k_w\|\sigma_n\|\mathrm{T}\hat{w}, \tag{25}$$

where T is a positive constant. The weight error $\tilde{w}$ and sliding surface σ_n are constrained by

$$\left. \begin{array}{l} \|\sigma_n\| > \left(\dfrac{(k_w w_m^2/4) - \|\gamma_2\| - \|\alpha_1\|\|\xi\|}{(\gamma_1)_{\min}}\right), \\ \|\tilde{w}\|_F > \dfrac{w_m}{2} + \sqrt{\dfrac{k_w w_m^2}{4} - \|\gamma_2\| - \|\alpha_1\|\|\xi\|}. \end{array} \right. \tag{26}$$

Proof. Take into account the following Lyapunov function candidate:

$$V = \frac{1}{2}\sigma_n^T\sigma_n + \frac{1}{2}\tilde{w}^T\mathrm{T}^{-1}\tilde{w}, \tag{27}$$

where $\tilde{w} = w - \hat{w}$ and $\dot{\tilde{w}} = -\dot{\hat{w}}$.

Differentiating equation (27)

$$\dot{V} = \sigma_n^T\dot{\sigma}_n - \tilde{w}^T\mathrm{T}^{-1}\dot{\hat{w}}. \tag{28}$$

Using equations (21) and (28)

$$\left. \begin{array}{l} \dot{V} = \sigma_n^T\left[\alpha_1\ddot{\hat{x}}(t) - (\alpha_1 A - \alpha_1 B\alpha_2)\dot{\hat{x}}(t) + \Upsilon\left\{\alpha_1\dot{\hat{x}}(t) - (\alpha_1 A - \alpha_1 B\alpha_2)\hat{x}(t)\right\}\right] - tr\left(\tilde{w}^T\Gamma^{-1}\dot{\tilde{w}}\right) \\ \dot{V} = \sigma_n^T\left[\alpha_1\left\{A\dot{\hat{x}}(t) + B\dot{x}(t) + \dot{d}(t)\right\} - (\alpha_1 A - \alpha_1 B\alpha_2)\dot{\hat{x}}(t) + \Upsilon\left\{\alpha_1\dot{\hat{x}}(t) - (\alpha_1 A - \alpha_1 B\alpha_2)\hat{x}(t)\right\}\right] - tr\left(\tilde{w}^T\Gamma^{-1}\dot{\tilde{w}}\right) \\ \dot{V} = \sigma_n^T\left[\alpha_1\left\{B\dot{u}(t) + \dot{d}(t)\right\} + \alpha_1 B\alpha_2\dot{\hat{x}}(t) + \Upsilon\dot{\sigma}(t)\right] - tr\left(\tilde{w}^T\Gamma^{-1}\dot{\tilde{w}}\right) \end{array} \right\}. \tag{29}$$

Substituting the control law equation (24) into equation (29)

$$\dot{V}(t) = \sigma_n^T(t)\left[-\|\alpha_1\|\dot{\widehat{d(t)}} - \alpha_1 B\alpha_2 \dot{\hat{x}}(t) - \Upsilon\sigma_n(t) - \gamma_1\sigma_n(t) - \gamma_2\mathrm{sgn}\{\sigma_n(t)\} + \|\alpha_1\|\dot{\widehat{d(t)}} + \alpha_1 B\alpha_2\dot{\hat{x}}(t) + \Upsilon\dot{\sigma}(t)\right] - tr\left(\tilde{w}^T \mathrm{T}^{-1}\dot{\hat{w}}\right)$$

$$\dot{V}(t) = \sigma_n^T(t)\left[-\|\alpha_1\|(\dot{\widehat{d(t)}} - \dot{\widehat{d(t)}}) - \gamma_1\sigma_n(t) - \gamma_2\mathrm{sgn}\{\sigma_n(t)\}\right] - tr\left(\tilde{w}^T \mathrm{T}^{-1}\dot{\hat{w}}\right) \tag{30}$$

Substituting equation (25) into equation (30)

$$\dot{V} \le \sigma_n^T(t)\left[-\|\alpha_1\|w^T\phi - \xi - \hat{w}^T\phi\} - \gamma_1\sigma_n(t) - \gamma_2\mathrm{sgn}\{\sigma_n(t)\}\right]$$
$$- tr\{\tilde{w}^T\mathrm{T}^{-1}\left(\|\alpha_1\|\mathrm{T}\phi\sigma_n^T - k_w\|\sigma_n\|\mathrm{T}\hat{w}\right)\}. \tag{31}$$

It is noted that $\sigma_n^T(t)\,\mathrm{sign}\,\sigma_n(t) = \|\sigma_n\|$ in equation (31). Owing to $\sigma_n^T(t)\gamma_1\sigma_n(t) = \|\sigma_n\|(\gamma_1)_{min}\|\sigma_n\|$, $(\gamma_1)_{min}$ is the minimum eigenvalue of γ_1. Equation (31) can be rewritten as follows:

$$\dot{V} \le \left[-\|\sigma_n\|(\gamma_1)_{min}\|\sigma_n\| - \|\gamma_2\|\|\sigma_n\| - \|\alpha_1\|\|\xi\|\|\sigma_n\| + \|\alpha_1\|\tilde{w}^T\phi\sigma_n^T\right] - tr\left(\tilde{w}^T\left(\|\alpha_1\|\phi\sigma_n^T - k_w\|\sigma_n\|\hat{w}\right)\right)$$

$$\dot{V} \le \left[-\|\sigma_n\|(\gamma_1)_{min}\|\sigma_n\| - \|\mu\|\|\sigma_n\| - \|\alpha_1\|\|\xi\|\|\sigma_n\|\right] + tr\left(k_w\|\sigma_n\|\tilde{w}^T\hat{w}\right) \tag{32}$$

The inequality is applied as given in the following equation:

$$tr\left(\tilde{w}^T(w - \tilde{w})\right) \le \|w\|_F\|\tilde{w}\|_F - \|\tilde{w}\|_F^2. \tag{33}$$

We get

$$\dot{V} \le -\|\sigma_n\|\left[(\gamma_1)_{min}\|\sigma_n\| + \|\gamma_2\| + \|\alpha_1\|\|\xi\| + k_w\|\tilde{w}\|_F(\|\tilde{w}\|_F - w_m)\right]$$

$$\dot{V} \le -\|\sigma_n\|\left[(\gamma_1)_{min}\|\sigma_n\| + \|\gamma_2\| + \|\alpha_1\|\|\xi\| + k_w\left(\|\tilde{w}\|_F - \frac{w_m}{2}\right)^2 - \frac{k_w w_m^2}{4}\right]$$

$$\|\sigma_n\| > \left(\frac{(k_w w_m^2/4) - \|\gamma_2\| - \|\alpha_1\|\|\xi\|}{(\gamma_1)_{min}}\right),$$

$$\|\tilde{w}\|_F > \frac{w_m}{2} + \sqrt{\frac{k_w w_m^2}{4} - \|\gamma_2\| - \|\alpha_1\|\|\xi\|}. \tag{34}$$

As a result, $\dot{V}$ (equation (34)) is negative outside of a compact set, demonstrating that it is uniformly ultimately bounded (UUB) of both $\|\sigma_n\|$ and $\|\tilde{w}\|_F$.

Harris hawk optimization (HHO) is applied to tune the parameter of SOSMC, which is given in next section. □

4. Harris Hawk Optimization (HHO)

The Harris hawk (HH) is one of the most intellectual and illustrious birds in nature with unique mass hunting skills in tracking, swirling, rinsing, and capturing potential animals (rabbits) in the group in search of food. The starting population here is supposed to be a crowd of hawks (solving optimization problems) trying to hunt the target rabbit with seven killing strategies from different directions. First, the leader hawk attempts to attack the prey. If the animal cannot be grabbed due to prey dynamism and escape behavior, switching tactics are performed to attack the escaped prey until another group will hit the escaped prey until caught. The key benefit of this tactic is that birds can chase pointed rabbits through the confusion and exhaustion of fleeing prey. Therefore, HHO indicates the exploration and exploitation stages, which are described in Figure 2 [33–35].

Step 1: Exploration Phase. The perch of the leader hawks is determined by the location of family members and prey. This is expressed as a mathematical equation for the change in distance between the hawks and the prey, as defined in the following equation:

$$Z(j+1) = \begin{cases} Z_{rand}(j) - r_1|Z_{rand}(j) - 2r_2 Z(j)|, & p_0 \ge 0.5, \\ Z_{rabbit}(j) - Z_m(j) - r_3(LB + r_4(UB - LB)), & p_0 < 0.5, \end{cases} \tag{35}$$

where $Z(j+1)$ is the updating vector of the Hawk's position at the $j+1$ iteration, $Z_r(j)$ is the position of the prey, $Z(j)$ is

the position vector of the hawks at the jth iteration, r_1, r_2, r_3, r_4, and p_0 are random numbers between 0 and 1, LB and UB are the lower and upper bounds of variables, and $Z_{ra}(j)$ and $Z_m(j)$ are the initial population assumed randomly.

The average position of each hawk is defined in the following equation:

$$Z_{i+1}(j) = \frac{1}{N} \sum_{i=1}^{N} Z_i(j), \quad (36)$$

where $Z_i(j)$ is the present location of hawks, $Z_{i+1}(j)$ is the updated location, and the total number of hawks is represented by N.

Step 2 During the exploration phase, the hawks attempt to locate and hit the prey. Due to this, there may be substantial alternate withinside the energy (E_e) of the prey and it is given in the following equation:

$$\text{Escaping Energy}, E_e = 2E_{eo}\left(1 - \frac{t_0}{\Gamma_0}\right), \quad (37)$$

where t_0 is the present iteration, Γ_0 is the maximum iteration count, and the starting energy (E_{eo}) varies randomly between −1 and 1 at each iteration. $E_e \geq 1$ shows prey's leaping behavior and the hawks are searching for prey in different location, and $E_e < 1$ suggests that the prey turns into exhausted.

Step 3 Exploitation Phase. At this point, the prey is attacked using a variety of strategies. When the prey is successfully fleeing from hawks, the probability of escaping is depicted as e_r, and when $e_r < 0.5$ and $e_r \geq 0.5$, the prey is successfully and unsuccessful escaped, respectively. If the prey escaped when $e_r \geq 0.5$, $|E_e| < 0.5$ and $e_r \geq 0.5$, $|E_e| \geq 0.5$, then a hard siege and soft siege occurs, respectively.

Step 4 Soft Siege (SS). Here, the rabbit possesses energy and attempts to escape by leaping and the hawks surround it softly, which is shown in the following equation:

$$\begin{aligned} Z(j+1) &= \Delta Z(j) - E|IZ_{\text{rabbit}}(j) - Z(j)|, \\ \Delta Z(j) &= Z_{\text{rabbit}}(j) - Z(j). \end{aligned} \quad (38)$$

The random jump of the rabbit is given by $I = 2(1 - r_5)$, where $\Delta Z(j)$ is the difference between the position of consecutive iteration and r_5 is the number n between 0 and 1.

Step 5 Hard Siege (HS). Here, the prey is completely exhausted and the hawks encircle it hardly. Equation (45) is used to update the positions, as shown in the following equation:

$$X(j+1) = X_{\text{rabbit}}(j) - E_e|\Delta X(j)|. \quad (39)$$

Step 6 Soft Siege with Consecutive Quick Dives. The rabbit still has energy and attempts to flee, which is depicted as $|E_e| \geq 0.5$ and $e_r < 0.5$; therefore, a soft siege is necessary

before the hawks' surprise pounce. This is a more intelligent step than the one before it. The Levy flight (LF) idea was developed here for progressive quick dives of hawks to execute a soft siege, with the hawks evaluating the prey's next move using the following equation:

$$Y = Z_{\text{rabbit}}(j) - E|IZ_{\text{rabbit}}(j) - Z_m(j)|. \quad (40)$$

Despite many efforts, the hawks evaluate each of their motions to the previous dive to decide whether it was a successful dive. It executes an uneven, sudden, and quick dive to reach the prey animal if the dive is not reasonable. We suppose the hawks dive based on LF-based patterns and use the following rule:

$$H = Y + S \times LF(M), \quad (41)$$

where M is the dimension of the problem and S is the random vector of size $1 \times M$.

The levy flight function (LF) can be demonstrated, as shown in the following equation:

$$\left. \begin{aligned} LF(z) &= 0.01 \times \frac{\mu \times \zeta}{|v|^{(1/\delta)}} \\ \therefore \zeta &= \left(\frac{\tau(1+\delta) \times \sin(\pi\delta/2)}{\tau(1+\delta/2) \times \delta \times 2^{(\delta-1/2)}} \right)^{1/\delta} \end{aligned} \right\}. \quad (42)$$

Here, μ and v are accidental values in the range (0, 1) and δ is a constant supposed to be equal to 1.5. As a result, in the soft siege phase, the final updating rule for the hawk's position is defined in the following equation:

$$Z(j+1) = \begin{cases} Y & f(Y) < f(Z(j)), \\ H & f(H) < f(Z(j)), \end{cases} \quad (43)$$

where Y and H are calculated using equations (40) and (41).

Step 7 Hard Siege with Continuous Quick Dives. In this situation $|E_e| < 0.5$, the prey animal loses energy and becomes fatigued. The hawks then employ a hard siege to close the distance between them and the prey, allowing them to kill the prey. The case updating rule is shown as follows:

$$Z(j+1) = \begin{cases} Y & f(Y) < f(Z(j)), \\ H & f(H) < f(Z(j)), \end{cases} \quad (44)$$

$$Y = Z_{\text{rabbit}}(j) - E|IZ_{\text{rabbit}}(j) - Z_m(j)|, \quad (45)$$

$$H = Y + S \times LF(M). \quad (46)$$

Y in equation (45) and H in equation (46) are the next positions for the new iteration until the prey is killed. The proposed approach is shown (Figure 4) in the form of HHO pseudocode [33].

A regulatory constraint (boundary) optimization problem can be used to describe the proposed frequency regulation problem. The optimum gains of NNO-SOSMC are explored, and by applying HHO, an integral time absolute error (ITAE)-based objective function is defined in

equation (47). ITAE-based objective function is chosen for parameter optimization as it concurrently improves both transient and steady-state performance. Moreover, to carry out an unbiased comparative study, an identical objective function as defined in [36] is chosen in this work and defined in equation (47).

Similar objective function defined in [36] has been deliberated in equation (47). The optimized parameters of NNO-SOSMC are $R, C,$ and Υ. Performing an empirical study, the above-said controller parameter boundary ranges are set as $\alpha_1 \in [0.01, 4]$, $\alpha_2 \in [0.01, 4]$, $\gamma_1 \in [0.01, 2]$ and $\gamma_2 \in [0.01, 1]$. To carry out the simulation, maximum iteration and population size are considered 100 and 25, respectively. The control settings are listed in Table 2.

$$ J = \int_0^t \left[\left| \Delta f_i \right| + \left| \Delta f_j \right| + \left| \Delta P_{tie_{ij}} \right| \right] t \, \mathrm{dt}. \tag{47} $$

The simulation outputs of the proposed optimization technique (HHO) are compared with other well-known optimization methods, as given in the next section.

5. Simulation Results

The control performance of NNO-based SOSMC under the LFC framework has been assessed for two- and four-area interconnected power systems. The robustness of the applied/suggested nonlinear controller against system uncertainties has been evaluated by assuming four different operating scenarios. Initially, the practicability of developed NNO in estimating system disturbance without SMC/SOSMC was studied for test system 1. To perform the simulation, the load perturbations in the areas are assumed to $\Delta P_{d1} = 0.08 p.u, \Delta P_{d2} = 0.06 p.u.$

Figure 5(a) shows the load disturbance profile applied to area 1. The estimated output of NNO is also ($\Delta P_{d1} = 0.08 p.u$) plotted on the same figure for better comparison. It is worth noting that NNO efficiently estimates the actual load profile within 0.6 sec, which establish the proficiency of the developed NNO. The frequency deviation (FD) and tie-line power deviation (T-LPD) of studied test system 1 with/without NNO are depicted in Figures 5(b) and 5(c), respectively. The estimation error is given in Figure 5(b).

To measure the effectiveness of the developed control strategy, the system dynamics have been measured considering the following simulation environments:

Case 1. A step load perturbations are applied to the test system 1 in the presence of GRC nonlinearity and an extensive comparative study is performed with HHO and other well-known optimization methods.

Case 2. A multiple load perturbation is applied simultaneously to test system 1 and dynamic performance of system compare with the proposed HHO-NNO-SOSMC and NN-ISMC [26] controller.

Case 3. A multiple load perturbation and wind power perturbation are simultaneously applied to test system 1 and

dynamic performance of system is compared with the proposed HHO-NNO-SOSMC and NN-ISMC controller.

Case 4. Lastly, the performance of controller is investigated under the four-area NIPS (test system 2).

Case 5. In this case, two step load perturbations $\Delta P_{d1} = 0.015 p.u,$ and $\Delta P_{d2} = 0.01 p.u$ at $t = 5$sec are applied simultaneously to the test system 1 in the presence of GRC nonlinearity to carry out a fair comparison with the result of reference [26]. The optimized parameters of NNO-SOSMC and minimum objective function value (ITAE) are computed with different optimization techniques for a population size of 25 and 100 iterations, respectively. The convergence characteristic of HHO is obtained and is compared with Figure 6(a). It is noteworthy from Figure 6(a) that HHO attains the global minimum solution quickly and gives the least minimum objective function value compared to SSA, CSA, DE, and PSO.

The dynamic performances of test system 1 using HHO-tuned NN-SOSMC are illustrated in Figures 6(b)–6(d). The outputs obtained with PSO based PID, NN-ISMC [26], and SSA/DE/CSA/PSO-tuned NNO-SOSMC are also plotted in Figures 6(b)–6(d) to quantify the effectiveness control methodology. Table 3 lists the time response measurements of Figures 6(b)–6(d).

It is apparent from Table 3 and Figures 6(b)–6(d) that HHO-tuned NNO-SOSMC yields better system outputs than SSA, DE, CSA, and PSO-tuned NNO-SOSMC controllers in terms of settling time and peak magnitude of system oscillations. As a result, it is possible to conclude that HHO is capable of obtaining improved near-optimal frequency and power deviations for the investigated test system. In the following investigation, HHO is only considered to optimize the controller parameters. The control effort of the controllers is given in Figure 6(f), where NNO-SOSMC shows less chattering in comparison to NN-ISMC [26].

Case 6. In this case, a multiple load perturbation given in Figure 7(a) is applied simultaneously to two-area NIPS with GRC and GDB nonlinearities. The dynamic performance NIPS after these perturbations is revealed in Figures 7(b)–7(d). The results show that the suggested HHO-NNO-SOSMC effectively reduces frequency oscillations in this scenario. Furthermore, the given controller provides a response with the least amount of peak overshoot and undershoot, as well as a short settling time. As a result, it is possible to conclude that HHO-NNO-SOSMC is superior to NN-ISMC [26]. The control effort and NN output of the controllers are shown in Figures 7(e) and 7(f), respectively.

Case 7. In this case, multiple load perturbation (Figure 7(a)) and wind power perturbation (Figure 8(a)) are simultaneously applied to NIPS. The dynamic performance of NIPS after these perturbations with HHO-NNO-SOSMC and NN-ISMC controller is plotted in Figures 8(b)–8(d). The frequency deviation with HHO-NNO-SOSMC is quicker with less undershoot and overshoot than with NN-ISMC, as shown in Figures 8(b)–8(c). The control effort and NN

Initialize the number of population (N) and iteration (Γ_0)
X_i $(i = 1, 2, 3 \ldots, N)$
while do
Evaluate the fitness value of hawks
Now, set X_r as the **optimal location** of rabbit
for $\left(\text{different hawk } (X_i)\right)$ **do**
update $Energy(E_e)$ and its jumping strength (I)
Initial $Energy (E_{e0}) = 2rand() - 1, I = 2(1 - rand())$
Update E_e
if $\left(|E_e| \geq 1\right)$ **then**
Exploration phase
if $\left(|E_e| < 1\right)$ **then**
if $(e_r \geq 0.5 \text{ and } |E_e| \geq 0.5$ **then**
Exploitation phase
Ss
elseif $(e_r \geq 0.5 \text{ and } |E_e| \geq 0.5$ **then**
Hs
elseif $(e_r < 0.5 \text{ and } |E_e| < 0.5$ **then**
Ss
elseif $(e_r < 0.5 \text{ and } |E_e| < 0.5$ **then**
Hs
Return best location of Z_{rabbit}

Figure 4: Pseudocode of proposed HHO.

Table 2: Controller design parameter.

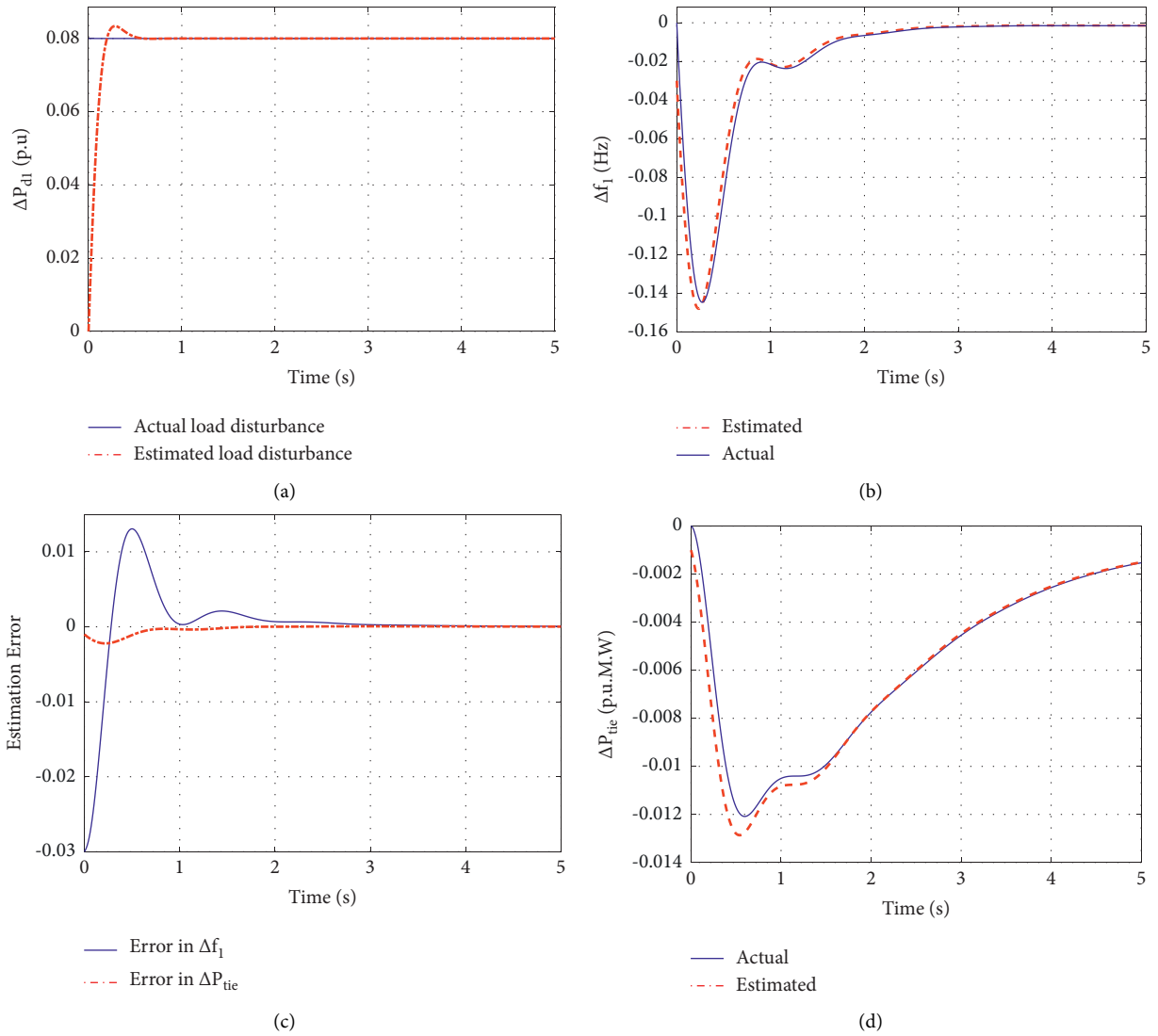|	
α_1	$\begin{bmatrix} 0.289 & 0.629 & 0.301 & 0.152 & 0.02 & 0.063 & 0.031 & 0.0188 & 0.51 & 0 & 0 & 0 & 0 \\ 0.156 & 0.118 & 0.108 & 1.018 & 0.023 & 0.941 & 0.123 & 0.042 & 1.237 & 0 & 0 & 0 & 0 \\ 0 & 0 & 0 & 0 & 0 & 0 & 0 & 0 & 0 & 2.109 & 0.701 & 0.329 & 0.026 \end{bmatrix}$
α_2	$\begin{bmatrix} 1.023 & 1.941 & 0.743 & 0.414 & 0.566 & 0.181 & 0.0287 & 1.188 & 1.237 & 0 & 0 & 0 & 0 \\ 0.566 & 0.181 & 0.028 & 1.188 & 1.023 & 1.941 & 0.7431 & 0.412 & 1.237 & 0 & 0 & 0 & 0 \\ 0 & 0 & 0 & 0 & 0 & 0 & 0 & 0 & 0 & 3.089 & 0.801 & 0.429 & 0.026 \end{bmatrix}$
γ_1	$diag(0.1 \ 0.2 \ 1.01)$
γ_2	$diag(0.12 \ 0.22 \ 0.01)$

(a)

(b)

(c)

(d)

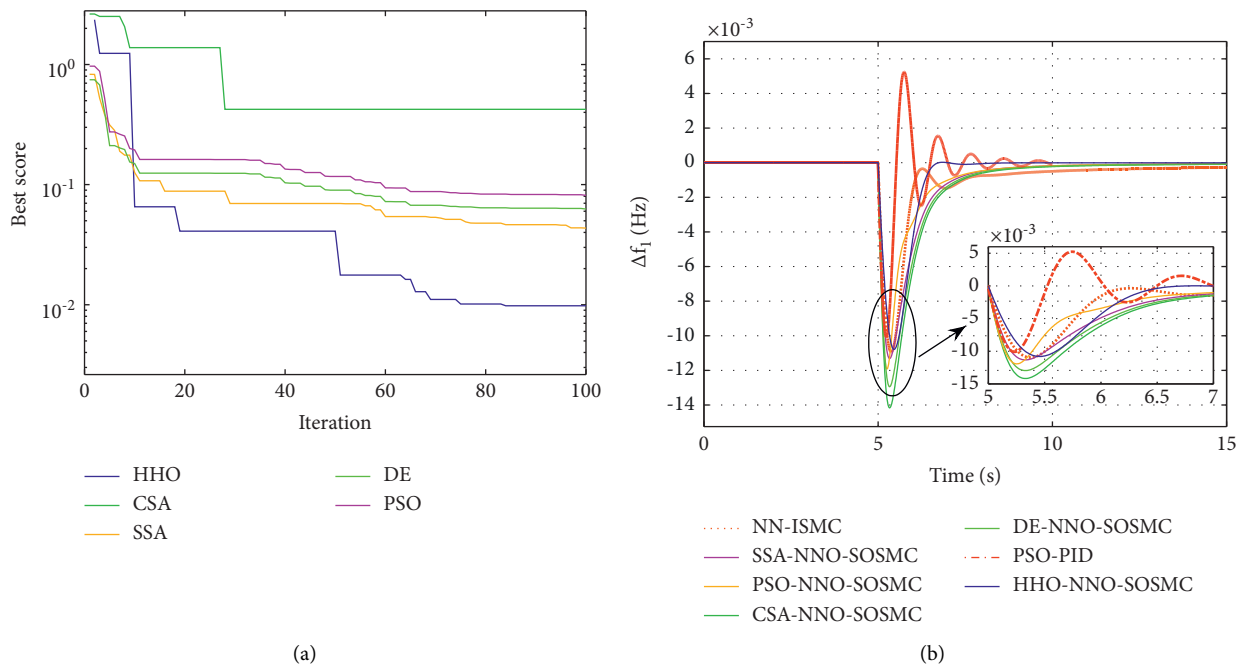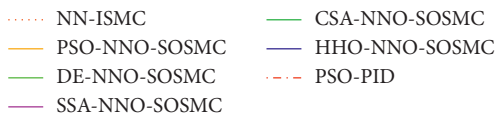FIGURE 5: (a) Actual and estimated disturbance. (b) Error in disturbance estimation. (c) FD in area 2. (d) T-LPD.

(a)

(b)

FIGURE 6: Continued.
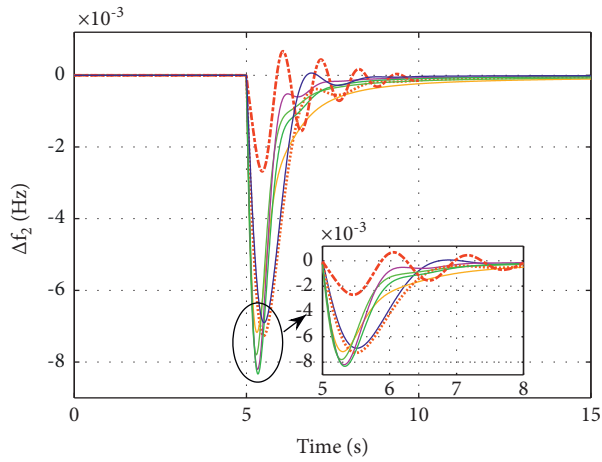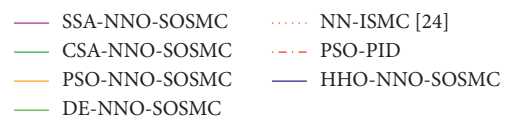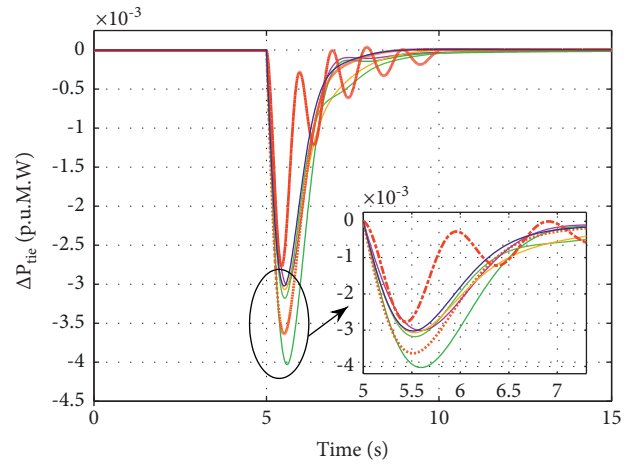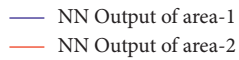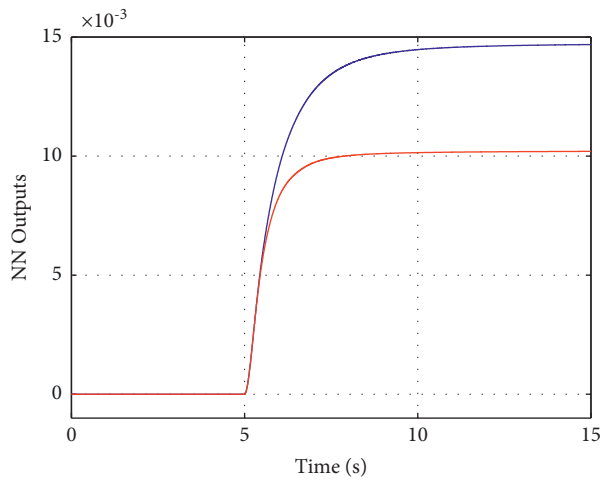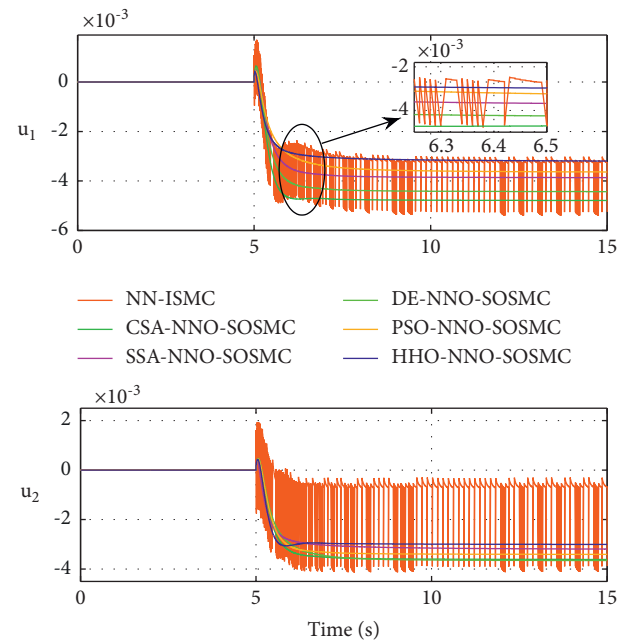
Figure 6: (a) Convergence profile of applied optimization techniques. (b) FD in area 1. (c) FD in area 2. (d) T-LPD. (e) NN outputs. (f) Control inputs.

TABLE 3: Comparison of transient analysis of NIPS with different optimization techniques.

Controllers	Δf_1		Δf_2		ΔP_{tie}		J
	Settling time (s)	Undershoot	Settling time (s)	Undershoot	Settling time (s)	Undershoot	
NN-ISMC [26]	9.646	0.0115	8.266	0.0073	8.62	0.0036	—
PSO-PID	9.91	0.010	10.52	0.003	10.02	0.028	0.55
HHO-NN-SOSMC	**6.615**	**0.0105**	**7.598**	**0.0066**	**8.14**	**0.003**	**0.02**
PSO-NN-SOSMC	10.212	0.0121	9.812	0.0067	10.12	0.0032	0.10
DE-NN-SOSMC	9.241	0.0131	10.12	0.0078	9.51	0.0033	0.08
CSA-NN-SOSMC	10.121	0.0142	9.89	0.0082	8.22	0.0040	0.42
SSA-NN-SOSMC	9.452	0.0122	7.621	0.0081	8.51	**0.003**	0.05

Bold faces show best results.
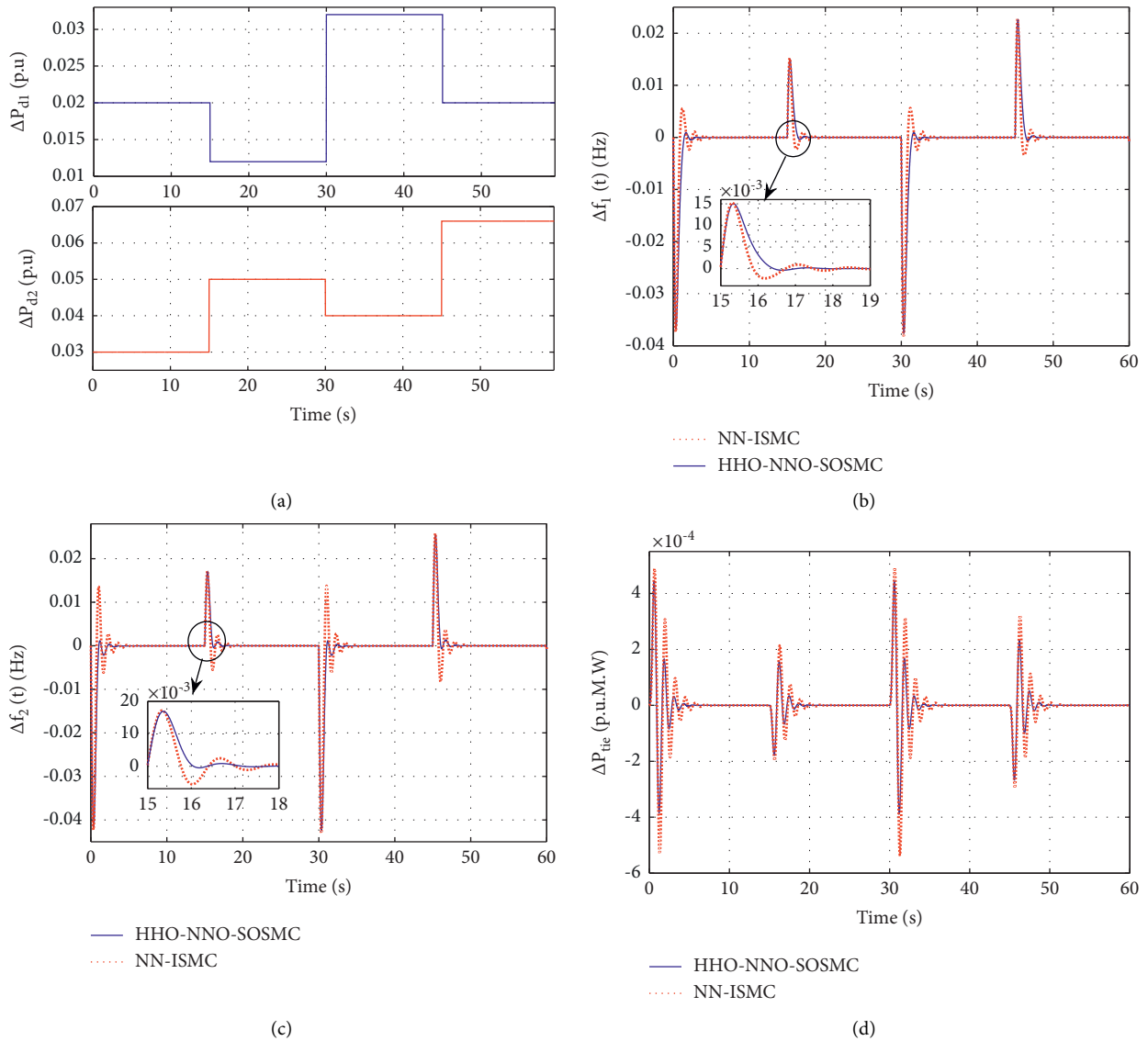

(a)

(b)

(c)
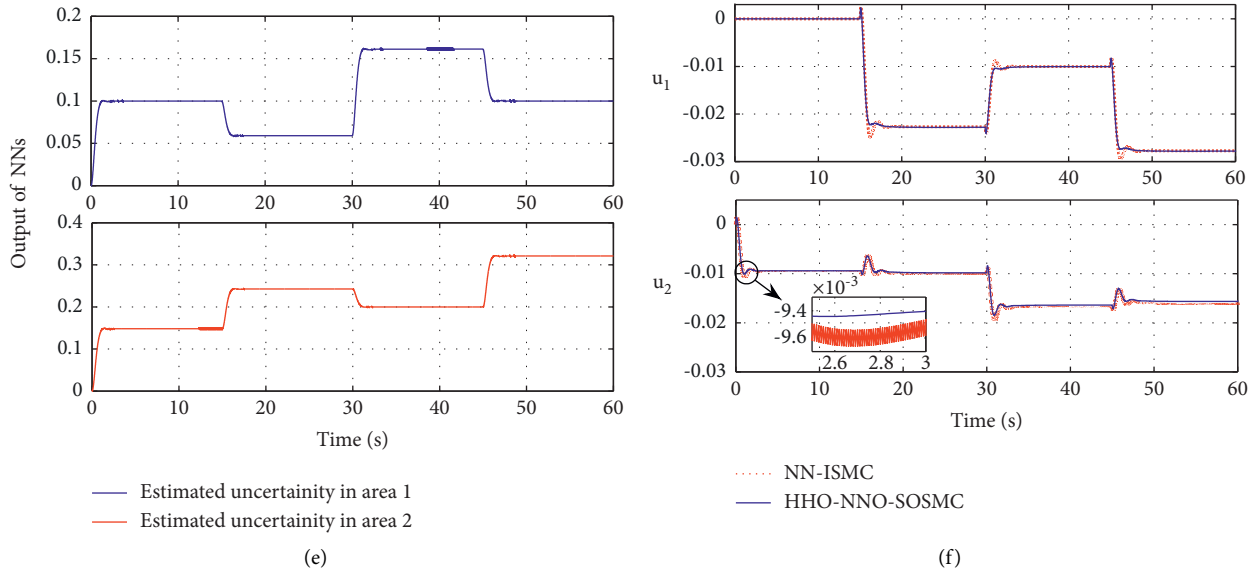
(d)

FIGURE 7: Continued.

(e)

(f)

Figure 7: (a) Load profile. (b) FD in area 1. (c) FD in area 2. (d) T-LPD. (e) Output of NN. (f) Control inputs.
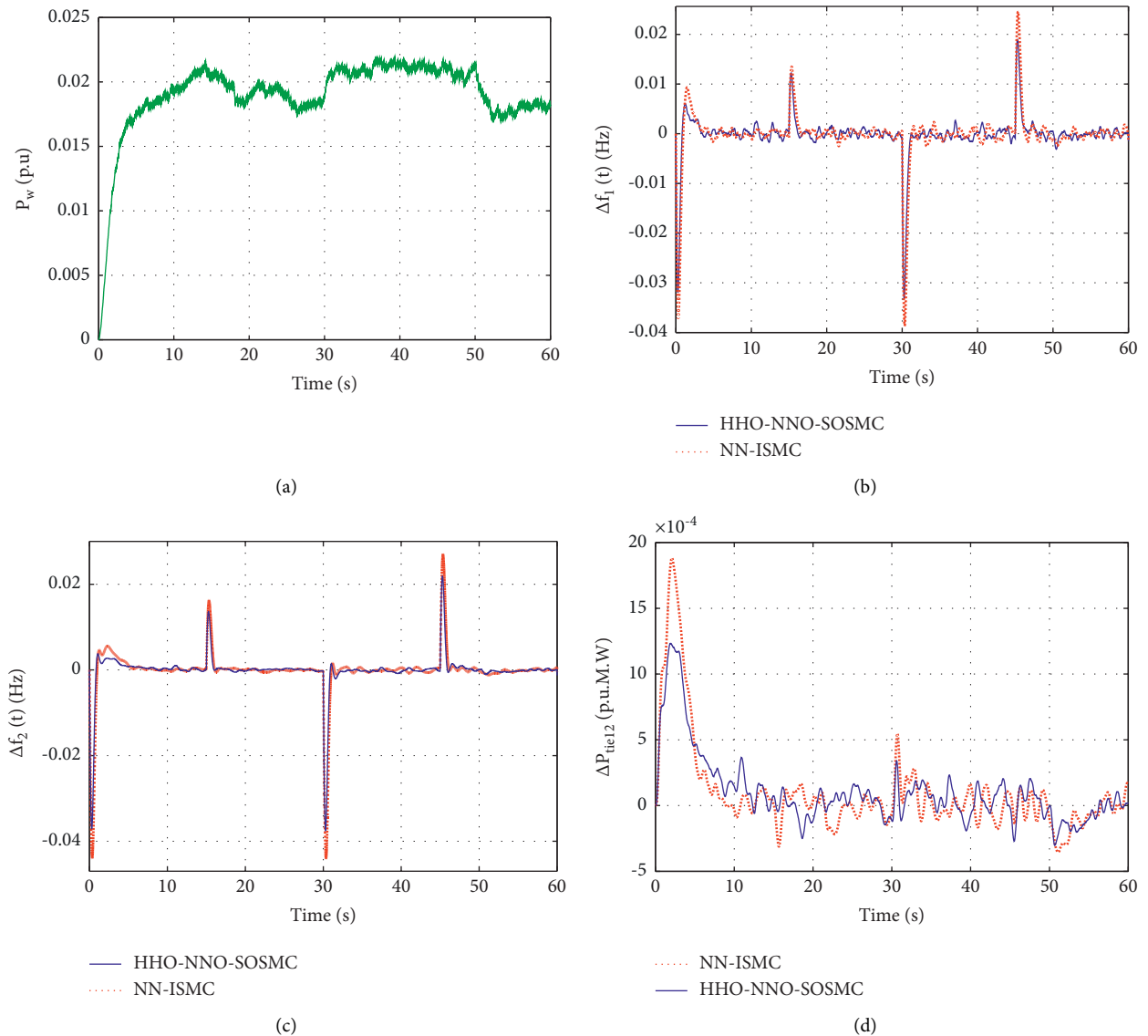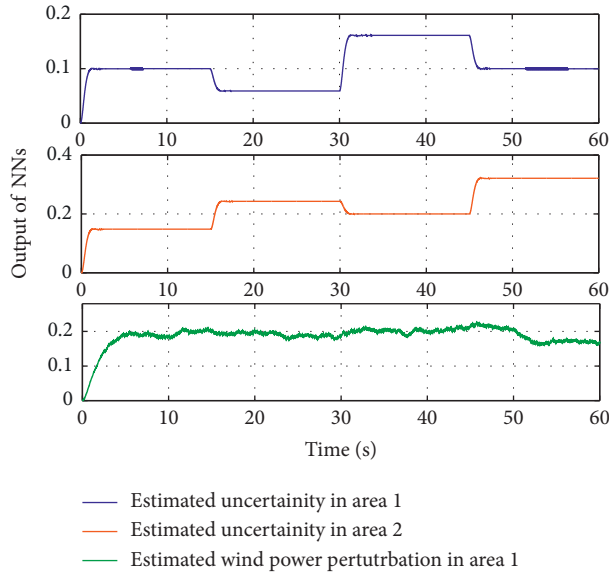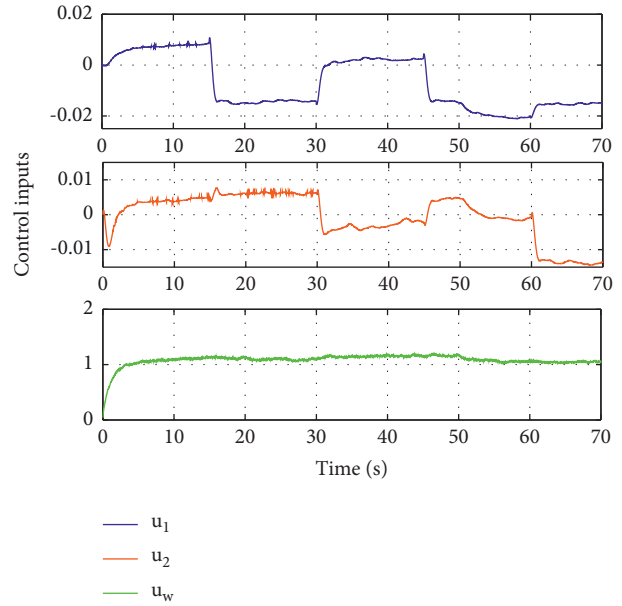

(a)

(b)

(c)

(d)

Figure 8: Continued.

(e)

(f)

Figure 8: (a) Wind power disturbance pattern. (b) FD in area 1. (c) FD in area 2. (d) T-LPD. (e) Output of NN. (f) Control inputs.
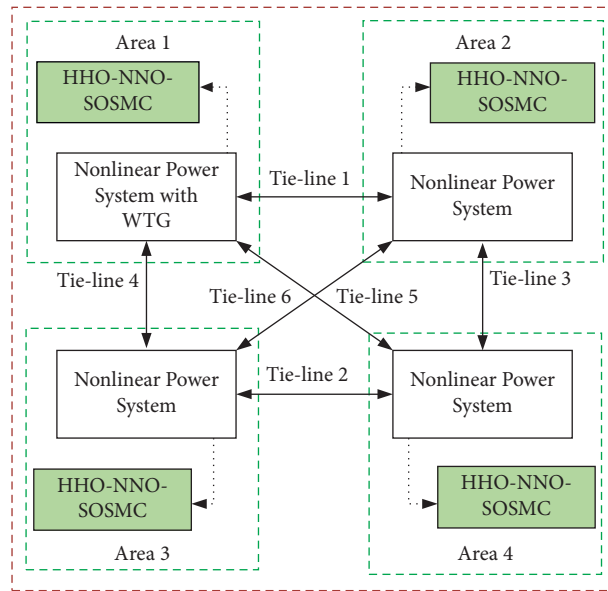

Figure 9: Four-area NIPS (test system 2).

output of the controllers are given in Figures 8(e) and 8(f), respectively.

Case 8. The performance of controller is investigated under the four-area IPS, as shown in Figure 9. In this case, multiple load perturbation (Figure 7(a)) in area 1 and area 2 and random wind power perturbation (Figure 8(a)) in

area 1 are simultaneously applied to 4-area IPS. The dynamic performance of 4-area NIPS after these perturbations is plotted in Figures 10(a)–10(b). The obtained results of HHO-NN-SOSMC controller are compared reported work [26] to demonstrate the superiority of the HHO-NN-SOSMC controller. It is revealed from Figures 10(a)–10(b) that frequency deviation with HHO-
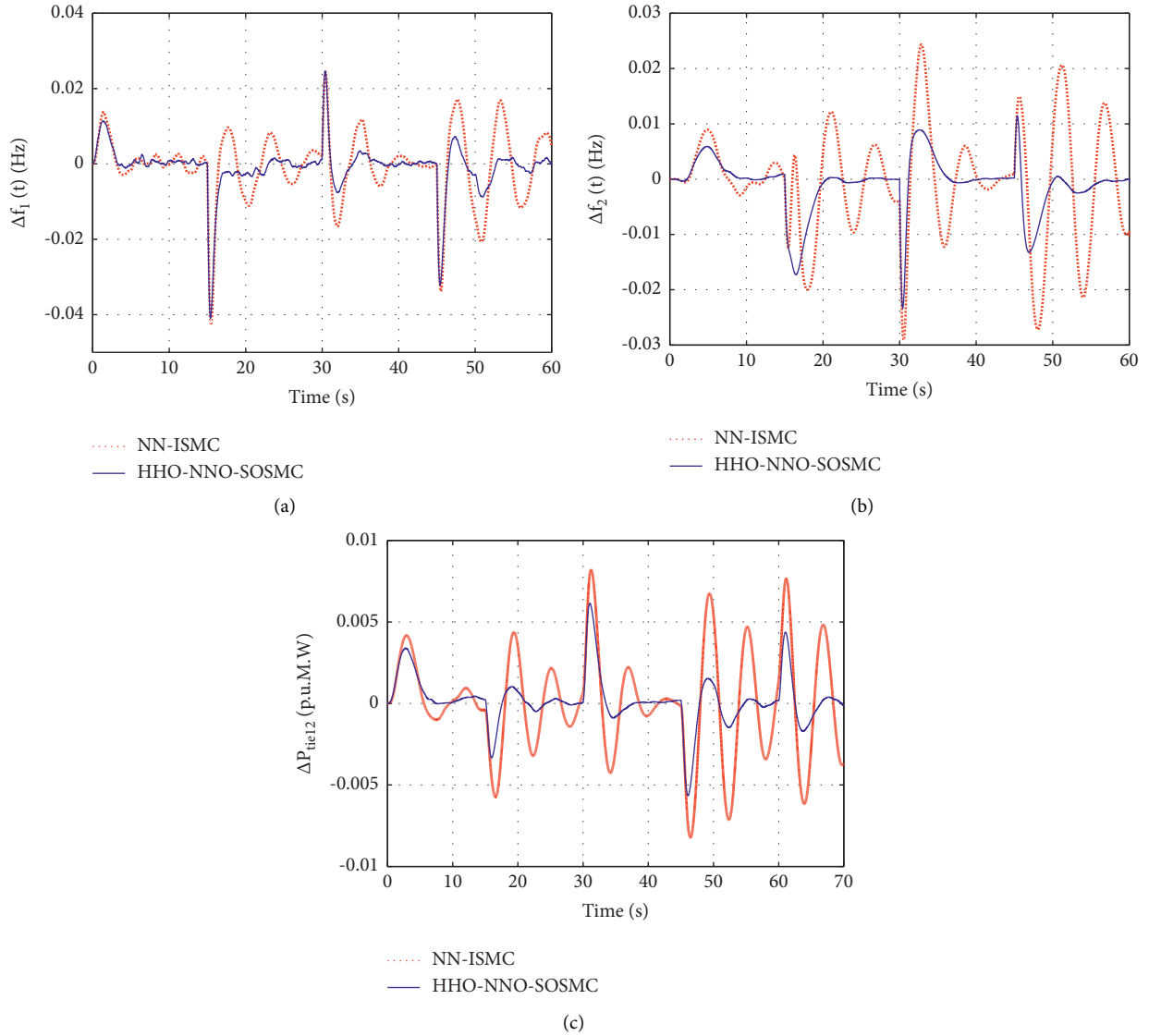
Figure 10: (a) FD in area-1. (b) FD in area-2. (c) T-LPD 12. (d) T-LPD 31.

NNO-SOSMC reaches the steady-state level with minimum undershoot and significantly faster as compared to other controllers.

6. Conclusion

This study presents the neural network observer (NNO)-based resilient frequency controller for nonlinear interconnected power systems. An NNO is developed to estimate unmodelled system dynamics and exogenous disturbances. An optimized second-order sliding mode control (SOSMC), augmented with the estimated output of NNO, is applied to regulate frequency outputs of the studied power systems against unknown and uncertain plant disturbances. The

design parameters of SOSMC are obtained using Harris hawk optimization and compared with other well-known optimization techniques to measure its tuning competence. Simulation results infer that HHO-NNO-SOSMC has minimum integral time absolute error value (0.02) and settling time (6.615 s) compared to other control techniques for Case 1. It also attenuates the chattering better than NNO-based integral SMC. In addition, the disturbance rejection ability and robust stability degree of the developed closed-loop control system improve significantly with the proposed controller.

In the future, the controller performance will be evaluated considering communication delay in the system. Furthermore, advanced SMC's variants may be developed to further reduce chattering while maintaining a closed-loop stability.

Appendix

$$A = \begin{bmatrix}
-\dfrac{1}{T_{p1}} & \dfrac{K_{p1}}{T_{p1}} & 0 & 0 & 0 & 0 & 0 & 0 & \dfrac{K_{p1}}{T_{p1}} & 0 & 0 & 0 & 0 \\[2ex]
-\dfrac{n_2}{R_1 T_{g1} T_{t1}} & -\dfrac{1}{T_{t1}} & \dfrac{1}{T_{t1}} & \dfrac{n_2}{T_{g1} T_{t1}} & 0 & 0 & 0 & 0 & 0 & 0 & 0 & 0 & 0 \\[2ex]
-\left\{n_1 - \dfrac{n_2}{T_{g1}}\right\}\dfrac{1}{R_1 T_{g1}} & 0 & -\dfrac{1}{T_{g1}} & -\left\{n_1 - \dfrac{n_2}{T_{g1}}\right\}\dfrac{1}{T_{g1}} & 0 & 0 & 0 & 0 & 0 & 0 & 0 & 0 & 0 \\[2ex]
K_1 B_1 & 0 & 0 & 0 & 0 & 0 & 0 & 0 & K_{\theta 1} & 0 & 0 & 0 & 0 \\[2ex]
0 & 0 & 0 & 0 & \dfrac{1}{T_{p2}} & \dfrac{K_{p2}}{T_{p2}} & 0 & 0 & \dfrac{K_{p2}}{T_{p2}} & 0 & 0 & 0 & 0 \\[2ex]
0 & 0 & 0 & 0 & \dfrac{n_2}{R_2 T_{g2} T_{t2}} & -\dfrac{1}{T_{t2}} & \dfrac{1}{T_{t2}} & -\dfrac{n_2}{T_{g2} T_{t2}} & 0 & 0 & 0 & 0 & 0 \\[2ex]
0 & 0 & 0 & 0 & -\left\{n_1 - \dfrac{n_2}{T_{g2}}\right\}\dfrac{1}{R_2 T_{g2}} & 0 & -\dfrac{1}{T_{g2}} & -\left\{n_1 - \dfrac{n_2}{T_{g2}}\right\}\dfrac{1}{T_{g2}} & 0 & 0 & 0 & 0 & 0 \\[2ex]
0 & 0 & 0 & 0 & K_{i2} B_2 & 0 & 0 & 0 & -K_{e2} & 0 & 0 & 0 & 0 \\[2ex]
2\pi T_0 & 0 & 0 & 0 & -2\pi T_0 & 0 & 0 & 0 & 0 & 0 & 0 & 0 & 0 \\[2ex]
0 & 0 & 0 & 0 & 0 & 0 & 0 & 0 & 0 & \dfrac{-(B_t + B_{sh})}{J_t} & \dfrac{B_{sh}}{J_t} & -\dfrac{1}{J_t} & 0 \\[2ex]
0 & 0 & 0 & 0 & 0 & 0 & 0 & 0 & 0 & \dfrac{D_{sh}}{2J_g} & \dfrac{-(B_g + B_{sh})}{J_g} & \dfrac{1}{N_g J_g} & \dfrac{1}{J_g} \\[2ex]
0 & 0 & 0 & 0 & 0 & 0 & 0 & 0 & 0 & K_{sh} & \dfrac{K_{sh}}{N_R} & 0 & 0 \\[2ex]
0 & 0 & 0 & 0 & 0 & 0 & 0 & 0 & 0 & 0 & 0 & 0 & -\dfrac{1}{r_g}
\end{bmatrix}$$

$$\text{(A.1)}$$

$$A = \begin{bmatrix}
-\dfrac{1}{T_{p1}} & \dfrac{K_{p1}}{T_{p1}} & 0 & 0 & 0 & 0 & 0 & 0 & \dfrac{K_{p1}}{T_{p1}} & 0 & 0 & 0 & 0 \\[2ex]
\dfrac{n_2}{R_1 T_{g1} T_{t1}} & -\dfrac{1}{T_{t1}} & \dfrac{1}{T_{t1}} & -\dfrac{n_2}{T_{g1} T_{t1}} & 0 & 0 & 0 & 0 & 0 & 0 & 0 & 0 & 0 \\[2ex]
-\left\{n_1 - \dfrac{n_2}{T_{g1}}\right\}\dfrac{1}{R_1 T_{g1}} & 0 & -\dfrac{1}{T_{g1}} & -\left\{n_1 - \dfrac{n_2}{T_{g1}}\right\}\dfrac{1}{T_{g1}} & 0 & 0 & 0 & 0 & 0 & 0 & 0 & 0 & 0 \\[2ex]
K_1 B_1 & 0 & 0 & 0 & 0 & 0 & 0 & 0 & K_{\theta 1} & 0 & 0 & 0 & 0 \\[2ex]
0 & 0 & 0 & 0 & -\dfrac{1}{T_{p2}} & \dfrac{K_{p2}}{T_{p2}} & 0 & 0 & \dfrac{K_{p2}}{T_{p2}} & 0 & 0 & 0 & 0 \\[2ex]
0 & 0 & 0 & 0 & -\dfrac{n_2}{R_2 T_{g2} T_{t2}} & -\dfrac{1}{T_{t2}} & \dfrac{1}{T_{t2}} & -\dfrac{n_2}{T_{g2} T_{t2}} & 0 & 0 & 0 & 0 & 0 \\[2ex]
0 & 0 & 0 & 0 & -\left\{n_1 - \dfrac{n_2}{T_{g2}}\right\}\dfrac{1}{R_2 T_{g2}} & 0 & -\dfrac{1}{T_{g2}} & -\left\{n_1 - \dfrac{n_2}{T_{g2}}\right\}\dfrac{1}{T_{g2}} & 0 & 0 & 0 & 0 & 0 \\[2ex]
0 & 0 & 0 & 0 & K_{i2} B_2 & 0 & 0 & 0 & -K_{e2} & 0 & 0 & 0 & 0 \\[2ex]
2\pi T_0 & 0 & 0 & 0 & -2\pi T_0 & 0 & 0 & 0 & 0 & 0 & 0 & 0 & 0 \\[2ex]
0 & 0 & 0 & 0 & 0 & 0 & 0 & 0 & 0 & \dfrac{-(B_t + B_{sh})}{J_t} & \dfrac{B_{sh}}{J_t} & -\dfrac{1}{J_t} & 0 \\[2ex]
0 & 0 & 0 & 0 & 0 & 0 & 0 & 0 & 0 & \dfrac{D_{sh}}{2J_g} & \dfrac{-(B_g + B_{sh})}{J_g} & \dfrac{1}{N_g J_g} & -\dfrac{1}{J_g} \\[2ex]
0 & 0 & 0 & 0 & 0 & 0 & 0 & 0 & 0 & K_{sh} & -\dfrac{K_{sh}}{N_R} & 0 & 0 \\[2ex]
0 & 0 & 0 & 0 & 0 & 0 & 0 & 0 & 0 & 0 & 0 & 0 & -\dfrac{1}{r_g}
\end{bmatrix},$$

$$D = \begin{bmatrix}
-\dfrac{K_{p1}}{T_{p1}} & 0 & 0 & 0 & 0 & 0 & 0 & 0 & 0 & 0 & 0 & 0 & 0 \\[2ex]
0 & 0 & 0 & 0 & -\dfrac{K_{p2}}{T_{p2}} & 0 & 0 & 0 & 0 & 0 & 0 & 0 & 0 \\[2ex]
\dfrac{K_{p1}}{T_{p1}} & 0 & 0 & 0 & 0 & 0 & 0 & 0 & 0 & 0 & 0 & 0 & 0 \\[2ex]
0 & 0 & 0 & 0 & 0 & 0 & 0 & 0 & \dfrac{1}{J_t} & 0 & 0 & 0
\end{bmatrix}^T,$$

$$B = \begin{bmatrix}
0 & \dfrac{n_2}{T_{g1} T_{t1}} & \left\{n_1 - \dfrac{n_2}{T_{g1}}\right\}\dfrac{1}{T_{g1}} & 0 & 0 & 0 & 0 & 0 & 0 & 0 & 0 & 0 \\[2ex]
0 & 0 & 0 & 0 & 0 & \dfrac{n_2}{T_{g2} T_{t2}} & \left\{n_1 - \dfrac{n_2}{T_{g2}}\right\}\dfrac{1}{T_{g2}} & 0 & 0 & 0 & 0 & 0 \\[2ex]
0 & 0 & 0 & 0 & 0 & 0 & 0 & 0 & 0 & 0 & 0 & \dfrac{1}{\tau_g}
\end{bmatrix}^T,$$

$$\Delta P = \begin{bmatrix} \Delta P_{d1} & \Delta P_{d2} & P_g & T_r \end{bmatrix}^T, u = \begin{bmatrix} u_1 & u_2 & u_w \end{bmatrix}^T.$$

$$\text{(A.2)}$$

A. Wind Aerodynamic Parameters

$\rho = 1.3 \, \text{kg/m}^3$, $A_b = 8505 \, \text{m}^2$, $\lambda_{opt} = 8.68$, $\theta = 1°$, $c_1 = 0.5$, $c_2 = 115$,, $c_3 = 0.38$,, $c_4 = 5$,, $c_5 = 21$, $c_6 = 0.007$.

B. Coupling Shaft

$J_t = 4.29 \, \text{s}$, $J_g = 0.9 \, \text{s}$, $B_t = B_g = 0$, $B_{sh} = 1.5$ pu, $\tau_g = 0.1$, $K_{sh} = 296.7$ pu, $N_g = 20$, $P_{w_{\text{base}}} = 3.6 \, \text{MW}$.

Data Availability

The results presented in the article are original. No data sheet has been considered to carry out the simulations study.

Conflicts of Interest

The authors declare that they have no conflicts of interest.

References

[1] M. Gheisarnejad and M. H. Khooban, "Secondary load frequency control for multi-microgrids: HiL real-time simulation," *Soft Computing*, vol. 23, pp. 5785–5798, 2019.

[2] P. Bajpai and V. Dash, "Hybrid renewable energy systems for power generation in stand-alone applications: a review," *Renewable and Sustainable Energy Reviews*, vol. 16, 2012.

[3] S. Prasad, S. Purwar, and N. Kishor, "Non-linear sliding mode control for frequency regulation with variable-speed wind turbine systems," *International Journal of Electrical Power and Energy Systems*, vol. 107, pp. 19–33, 2019.

[4] T. Senjyu, T. Nakaji, K. Uezato, and T. Funabashi, "A hybrid power system using alternative energy facilities in isolated Island," *IEEE Transactions on Energy Conversion*, vol. 20, no. 2, pp. 406–414, 2005.

[5] G. Shankar and V. Mukherjee, "Load frequency control of an autonomous hybrid power system by quasi-oppositional harmony search algorithm," *International Journal of Electrical Power & Energy Systems*, vol. 78, pp. 715–734, 2016.

[6] D. Guha, P. K. Roy, and S. Banerjee, "Optimal tuning of 3 degree-of-freedom proportional-integral-derivative controller for hybrid distributed power system using dragonfly algorithm," *Computers amd Electrical Engineering*, vol. 72, pp. 137–153, 2018.

[7] H. Bevrani, F. Habibi, P. Babahajyani, M. Watanabe, and Y. Mitani, "Intelligent frequency control in an AC microgrid: online PSO-based fuzzy tuning approach," *IEEE Transactions on Smart Grid*, vol. 3, no. 4, pp. 1935–1944, 2012.

[8] R. Lamba, S. K. Singla, and S. Sondhi, "Design of fractional order PID controller for load frequency control in perturbed two area interconnected system," *Electric Power Components and Systems*, vol. 47, pp. 998–1011, 2019.

[9] I. Pan and S. Das, "Fractional-order load-frequency control of interconnected power systems using chaotic multi-objective optimization," *Applied Soft Computing*, vol. 29, pp. 328–344, 2015.

[10] V. Patel, D. Guha, and S. Purwar, "Optimized cascade fractional-order 3DOF-controller for frequency regulation of a hybrid power system using marine predators algorithm," *International Journal of Numerical Modelling: Electronic Networks, Devices and Fields*, Article ID e3025, 2022.

[11] I. Kocaarslan and E. Çam, "Fuzzy logic controller in interconnected electrical power systems for load–frequency control," *International Journal of Electrical Power & Energy Systems*, vol. 27, no. 8, pp. 542–549, 2005.

[12] S. K. Pandey, N. Kishor, and S. R. Mohanty, "Frequency regulation in hybrid power system using iterative proportional -integral-derivative H_∞ Controller," *Electric Power Components and Systems*, vol. 42, no. 2, pp. 132–148, 2014.

[13] A. G. Pillai and E. Rita Samuel, "PSO based LQR-PID output feedback for load frequency control of reduced power system model using balanced truncation," *International Transactions On Electrical Energy Systems*, vol. 31, no. 9, Article ID e13012, 2021.

[14] Y. Mi, X. He, X. Hao et al., "Frequency control strategy of multi-area hybrid power system based on frequency division and sliding mode algorithm," *IET Generation, Transmission and Distribution*, vol. 13, no. 7, pp. 1145–1152, 2019.

[15] Z. Al-Hamouz, M. Zakariya, and H. N. Al-Duwaish, "A new load frequency variable structure controller using genetic algorithms," *Electric Power Systems Research*, vol. 55, no. 1, pp. 1–6, 2000.

[16] A. E. Onyeka, Y. Xing-Gang, Z. Mao, B. Jiang, and Q. Zhang, "Robust decentralised load frequency control for interconnected time delay power systems using sliding mode techniques," *IET Control Theory and Applications*, vol. 14, no. 3, pp. 470–480, 2020.

[17] C. Wang, Y. Mi, Y. Fu, and P. Wang, "Frequency control of an isolated micro-grid using double sliding mode controllers and disturbance observer," *IEEE Transactions on Smart Grid*, vol. 9, no. 2, pp. 923–930, 2018.

[18] Y. Mi, Y. Fu, C. Wang, and P. Wang, "Decentralized sliding mode load frequency control for multi-area power systems," *IEEE Transactions on Power Systems*, vol. 28, no. 4, pp. 4301–4309, Nov, 2013.

[19] S. Prasad, S. Purwar, and N. Kishor, "Non-linear sliding mode load frequency control in multi-area power system," *Control Engineering Practice*, vol. 61, pp. 81–92, 2017.

[20] V. Patel, D. Guha, and S. Purwar, "Microgrids," *Chapter 2 -Disturbance Observer–Aided Adaptive Sliding Mode Controller for Frequency Regulation in Hybrid Power System*, Academic Press, Cambridge, MA, USA, 2022.

[21] Y. Mi, Y. Fu, D. Li, C. Wang, P. C. Loh, and P. Wang, "The sliding mode load frequency control for hybrid power system based on disturbance observer," *International Journal of Electrical Power and Energy Systems*, vol. 74, pp. 446–452, 2016.

[22] A. Dev, S. Anand, and M. K. Sarkar, "Nonlinear disturbance observer based adaptive super twisting sliding mode load frequency control for nonlinear interconnected power network," *Asian Journal of Control*, vol. 23, no. 5, pp. 2484–2494, 2021.

[23] V. V. Huynh, P. T. Tran, T. M. Nguyen, V. D. Phan, and V. T. Pham, "Advanced sliding mode observer design for load frequency control of multiarea multisource power systems," *International Transactions on Electrical Energy Systems*, vol. 2022, Article ID 6587194, 21 pages, 2022.

[24] M. K. Sarkar, A. Dev, P. Asthana, and D. Narzary, "Chattering free robust adaptive integral higher order sliding mode control for load frequency problems in multi-area power systems," *IET Control Theory and Applications*, vol. 12, no. 9, pp. 1216–1227, 2018.

[25] D. Qian and G. Fan, "Neural-network-based terminal sliding mode control for frequency stabilization of renewable power systems," *IEEE/CAA Journal of Automatica Sinica*, vol. 5, no. 3, pp. 706–717, 2018.

[26] D. Qian, S. Tong, H. Liu, and X. Liu, "Load frequency control by neural-network-based integral sliding mode for nonlinear power systems with wind turbines," *Neurocomputing*, vol. 173, pp. 875–885, 2016.

[27] S. Prasad and M. R. Ansari, "Frequency regulation using neural network observer based controller in power system," *Control Engineering Practice*, vol. 102, Article ID 104571, 2020.

[28] V. Patel, D. Guha, and S. Purwar, "Neural network aided fractional-order sliding mode controller for frequency regulation of nonlinear power systems," *Computers and Electrical Engineering*, vol. 96, 2021.

[29] F. A. Shaik, S. Purwar, and B. Pratap, "Real-time implementation of Chebyshev neural network observer for twin rotor control system," *Expert Systems with Applications*, vol. 38, no. 10, pp. 13043–13049, 2011.

[30] C. M. Kwan and F. L. Lewis, "Robust backstepping control of induction motors using neural networks," *IEEE Transactions on Neural Networks*, vol. 11, no. 5, 2000.

[31] A. Malinowski, J. M. Zurada, and J. H. Lilly, "Inverse control of nonlinear systems using neural network observer and inverse mapping approach," *Proceedings of ICNN'95—International Conference on Neural Networks*, vol. 5, pp. 2513–2518, 1995.

[32] S. Hoseini and M. Farrokhi, "Observer-based stabilisation of some non-linear non-minimum phase systems using neural network," *International Journal of Modelling, Identification and Control*, vol. 11, 2010.

[33] A. Abbasi, B. Firouzi, and P. Sendur, "On the application of Harris hawks optimization (HHO) algorithm to the design of microchannel heat sinks," *Engineering with Computers*, vol. 37, no. 2, pp. 1409–1428, 2019.

[34] A. A. Heidari, S. Mirjalili, H. Faris, I. Aljarah, M. Mafarja, and H. Chen, "Harris hawks optimization: algorithm and applications," *Future Generation Computer Systems*, vol. 97, pp. 849–872, 2019.

[35] M. Bhuyan, D. C. Das, and A. K. Barik, "Proficient power control strategy for combined solar gas turbine-wind turbine generator-biodiesel generator based two area interconnected microgrid employed with DC link using Harris's hawk optimization optimised tilt-integral-derivative controller," *International Journal of Numerical Modelling: Electronic Networks, Devices and Fields*, vol. 35, no. 4, Article ID e2991, 2022.

[36] M. Barakat, A. Donkol, H. F. A. Hamed, and G. M. Salama, "Harris hawks-based optimization algorithm for automatic LFC of the interconnected power system using PD-PI cascade control," *Journal of Electrical Engineering and Technology*, vol. 16, no. 4, pp. 1845–1865, 2021.